Quantum Monte Carlo calculations of electromagnetic transitions in ^{8}Be with meson-exchange currents derived from chiral effective field theory

S. Pastore[1],* R. B. Wiringa[2],† Steven C. Pieper[2],‡ and R. Schiavilla[3,4§]

[1]*Department of Physics and Astronomy, University of South Carolina, Columbia, South Carolina 29208*
[2]*Physics Division, Argonne National Laboratory, Argonne, Illinois 60439*
[3]*Theory Center, Jefferson Laboratory, Newport News, Virginia 23606*
[4]*Department of Physics, Old Dominion University, Norfolk, Virginia 23529*

(Dated: June 11, 2014)

We report quantum Monte Carlo calculations of electromagnetic transitions in ^{8}Be. The realistic Argonne v_{18} two-nucleon and Illinois-7 three-nucleon potentials are used to generate the ground state and nine excited states, with energies that are in excellent agreement with experiment. A dozen $M1$ and eight $E2$ transition matrix elements between these states are then evaluated. The $E2$ matrix elements are computed only in impulse approximation, with those transitions from broad resonant states requiring special treatment. The $M1$ matrix elements include two-body meson-exchange currents derived from chiral effective field theory, which typically contribute 20–30% of the total expectation value. Many of the transitions are between isospin-mixed states; the calculations are performed for isospin-pure states and then combined with empirical mixing coefficients to compare to experiment. Alternate mixings are also explored. In general, we find that transitions between states that have the same dominant spatial symmetry are in reasonable agreement with experiment, but those transitions between different spatial symmetries are often underpredicted.

PACS numbers: 21.10.Ky, 02.70.Ss, 23.20.Js, 27.20.+n

arXiv:1406.2343v1 [nucl-th] 9 Jun 2014

I. INTRODUCTION

We recently reported *ab initio* quantum Monte Carlo (QMC) calculations of magnetic moments and electromagnetic (EM) transitions in $A \leq 9$ nuclei [1]. In that work, the calculated magnetic moments and $M1$ transitions included corrections arising from EM two-body meson-exchange currents (MEC) derived in two different approaches: 1) a standard nuclear physics approximation (SNPA) [2, 3], and 2) the chiral effective theory (χEFT) formulation of Refs. [4–6]. Nuclear wave functions (w.f.'s) were obtained from a Hamiltonian consisting of the non-relativistic nucleon kinetic energy plus the Argonne v_{18} (AV18) two-nucleon [7] and Illinois-7 (IL7) three-nucleon [8] potentials. The SNPA MEC were constructed to obey current conservation with this Hamiltonian, while the use of χEFT MEC constitutes a hybrid calculation. The two methods are in substantial agreement, producing a theoretical microscopic description of nuclear dynamics that successfully reproduces the available experimental data, although the χEFT MEC give somewhat better results. Two-body components in the current operators provide significant corrections to single-nucleon impulse-approximation (IA) calculations. For example, they contribute up to $\sim 40\%$ of the total predicted value for the ^{9}C magnetic moment [1].

In this work, we implement the framework described above for twenty EM transitions in the ^{8}Be nucleus using only the χEFT MEC. The experimental spectrum and EM transitions we consider are illustrated in Fig. 1. This even-even nucleus exhibits a strong two-α cluster structure in its ground state, characterized by angular momentum, parity, and isospin $(J^\pi;T) = (0^+;0)$, and a Young diagram spatial symmetry that is predominantly [44]. The ground state lies ~ 0.1 MeV above the threshold for breakup into two α's, while the $(2^+;0)$ state at ~ 3 MeV excitation and $(4^+;0)$ state at ~ 11 MeV, are [44] rotational states with large ($\sim$ 1.5–3.5 MeV) decay widths. The next six higher states at 16–19 MeV excitation are three isospin-mixed doublets, with the first pair of $(2^+;0+1)$ states lying below the threshold for breakup into ^{7}Li+p and having $\alpha+\alpha$ decay widths of ~ 100 keV. The isospin mixing is due to the interplay between $T=0$ states and $T=1$ states that are the isobaric analogs of the lowest three states in ^{8}Li and ^{8}B, all with the same dominant [431] spatial symmetry. There are many additional broad excited states above these isospin-mixed doublets that are not shown before the final state we consider, the $(0^+;2)$ isobaric analog of the ^{8}He ground state at 27 MeV excitation, with dominant [422] spatial symmetry and a very narrow 5 keV decay width.

A comprehensive set of QMC calculations of $A = 8$ nuclei was carried out in Ref. [9] for a Hamiltonian with AV18 and the older Urbana IX three-nucleon potential [13]. More recently, energies, radii, and quadrupole moments of this nucleus have been recalculated for the [44] symmetry states [10], and for the isospin-mixed states [11], using the newer Illinois-7 potential. The present work complements these studies by calculating many EM transitions between the low-lying states, which

*Electronic address: pastores@mailbox.sc.edu
†Electronic address: wiringa@anl.gov
‡Electronic address: spieper@anl.gov
§Electronic address: schiavil@jlab.org

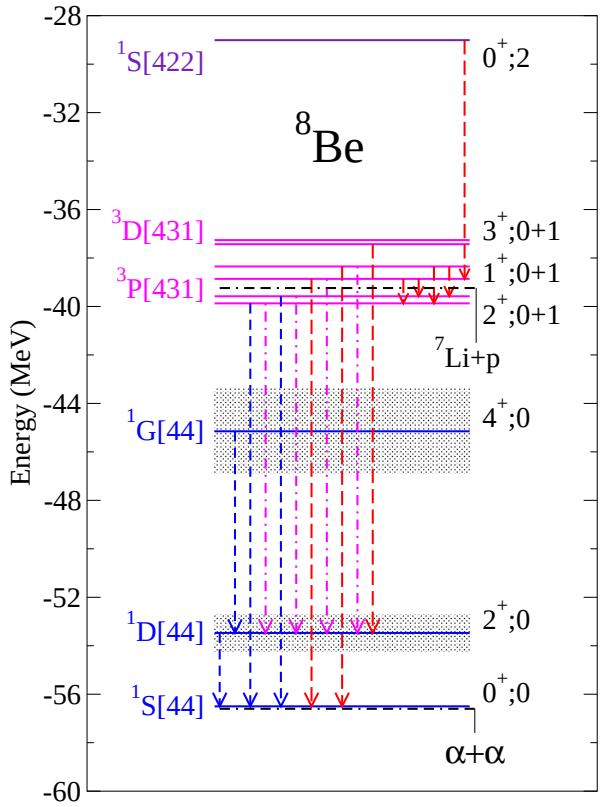

FIG. 1: (Color online) Experimental spectrum of ^{8}Be: horizontal lines denote energy levels, with blue for T=0 states, magenta for mixed T=0+1 states, and violet for T=2; black dash-dot lines indicate thresholds for breakup as indicated and shaded areas denote the large widths of the ^{8}Be rotational states. Vertical lines with arrows indicate the electromagnetic transitions studied: blue short-dash for $E2$, red long-dash for $M1$, and magenta dash-dot for combined $E2$ and $M1$ transitions.

are also illustrated in Fig. 1. The $M1$ matrix elements include contributions from two-body χEFT currents, which provide important corrections of order 20–30%. The two-body current corrections to the $E2$ matrix elements are expected to be negligible because they appear at higher order in the χEFT expansion [6] and are not computed here.

QMC techniques and χEFT EM currents were presented in Ref. [1] and references therein. We refer to that work for more details on the calculational scheme which is here briefly summarized in Sec. II. From there on, we focus on providing and discussing the results. In particular, the calculated ^{8}Be energy spectrum is presented in Sec. III, while results for $E2$ and $M1$ transitions are given in Sec. IV. We discuss the results in Sec. V.

II. QMC METHOD, NUCLEAR HAMILTONIAN AND χEFT EM CURRENTS

EM transition matrix elements are evaluated between w.f.'s which are solutions of the Schrödinger equation:

$$H\Psi(J^\pi;T,T_z) = E\Psi(J^\pi;T,T_z) \ , \qquad (1)$$

where $\Psi(J^\pi;T,T_z)$ is a nuclear w.f. with specific spin-parity J^π, isospin T, and charge state T_z. The nuclear Hamiltonian used in the calculations consists of a kinetic term plus two- and three-body interaction terms, namely the AV18 [7] and the IL7 [8], respectively:

$$H = \sum_i K_i + \sum_{i<j} v_{ij} + \sum_{i<j<k} V_{ijk} \ . \qquad (2)$$

Nuclear w.f.'s are constructed in two steps. First, a variational Monte Carlo (VMC) calculation is implemented to construct a trial w.f. $\Psi_V(J^\pi;T,T_z)$ from products of two- and three-body correlation operators acting on an antisymmetric single-particle state of the appropriate quantum numbers. The correlation operators are designed to reflect the influence of the interactions at short distances, while appropriate boundary conditions are imposed at long range [12, 13]. The $\Psi_V(J^\pi;T,T_z)$ has embedded variational parameters that are adjusted to minimize the expectation value

$$E_V = \frac{\langle\Psi_V|H|\Psi_V\rangle}{\langle\Psi_V|\Psi_V\rangle} \geq E_0 \ , \qquad (3)$$

which is evaluated by Metropolis Monte Carlo integration [14]. Here, E_0 is the exact lowest eigenvalue of H for the specified quantum numbers. A good variational trial function has the form

$$|\Psi_V\rangle = \mathcal{S}\prod_{i<j}^{A}\left[1+U_{ij}+\sum_{k\neq i,j}^{A}\widetilde{U}_{ijk}^{TNI}\right]|\Psi_J\rangle \ , \qquad (4)$$

where the $\mathcal{S}$ is a symmetrization operator. The Jastrow w.f. Ψ_J is fully antisymmetric and includes all possible spatial symmetry states within the p-shell that can contribute to the $(J^\pi;T,T_z)$ quantum numbers of the state of interest, while U_{ij} and $\widetilde{U}_{ijk}^{TNI}$ are the noncommuting two- and three-body correlation operators.

The second step improves on Ψ_V by eliminating excited-state contamination. This is accomplished by the Green's function Monte Carlo (GFMC) algorithm [15] which propagates the Schrödinger equation in imaginary time (τ). The propagated w.f. $\Psi(\tau) = e^{-(H-E_0)\tau}\Psi_V$, for large values of τ, converges to the exact w.f. with eigenvalue E_0. In practice, a simplified version H' of the Hamiltonian H is used in the operator, which includes the isoscalar part of the kinetic energy, a charge-independent eight-operator projection of AV18 called AV8′, a strength-adjusted version of the three-nucleon potential IL7′ (adjusted so that $\langle H'\rangle \sim \langle H\rangle$), and

an isoscalar Coulomb term that integrates to the total charge of the given nucleus [16]. The difference between H and H' is calculated using perturbation theory. More detail can be found in Refs. [9, 13].

Matrix elements of the operators of interest are evaluated in terms of a "mixed" expectation value between Ψ_V and $\Psi(\tau)$:

$$\langle O(\tau)\rangle_M \;=\; \frac{\langle\Psi(\tau)|O|\Psi_V\rangle}{\langle\Psi(\tau)|\Psi_V\rangle}, \tag{5}$$

where the operator O acts on the trial function Ψ_V. The desired expectation values, of course, have $\Psi(\tau)$ on both sides; by writing $\Psi(\tau) = \Psi_V + \delta\Psi(\tau)$ and neglecting terms of order $[\delta\Psi(\tau)]^2$, we obtain the approximate expression

$$\begin{aligned}\langle O(\tau)\rangle \;&=\; \frac{\langle\Psi(\tau)|O|\Psi(\tau)\rangle}{\langle\Psi(\tau)|\Psi(\tau)\rangle} \\ &\approx\; \langle O(\tau)\rangle_M + [\langle O(\tau)\rangle_M - \langle O\rangle_V]\;,\end{aligned} \tag{6}$$

where $\langle O\rangle_{\rm V}$ is the variational expectation value.

For off-diagonal matrix elements relevant to this work the generalized mixed estimate is given by the expression

$$\begin{aligned}&\frac{\langle\Psi^f(\tau)|O|\Psi^i(\tau)\rangle}{\sqrt{\langle\Psi^f(\tau)|\Psi^f(\tau)\rangle}\sqrt{\langle\Psi^i(\tau)|\Psi^i(\tau)\rangle}} \\ &\approx\; \langle O(\tau)\rangle_{M_i} + \langle O(\tau)\rangle_{M_f} - \langle O\rangle_V\;,\end{aligned} \tag{7}$$

where

$$\langle O(\tau)\rangle_{M_f} \;=\; \frac{\langle\Psi^f(\tau)|O|\Psi^i_V\rangle}{\langle\Psi^f(\tau)|\Psi^f_V\rangle}\sqrt{\frac{\langle\Psi^f_V|\Psi^f_V\rangle}{\langle\Psi^i_V|\Psi^i_V\rangle}}\;, \tag{8}$$

and $\langle O(\tau)\rangle_{M_i}$ is defined similarly. For more details see Eqs. (19–24) and the accompanying discussions in Ref. [17]. Sources of systematic error in the GFMC evaluation of operator expectation values (other than H') include the use of mixed estimates and the constrained path algorithm for controlling the Fermion sign problem in the propagation of $\Psi(\tau)$. These are discussed in Ref. [9]; the convergence of the current calculations is addressed at the beginning of Sec. III.

Nuclear EM currents are expressed as an expansion in many-body operators. The current we use contains up to two-body effects, and is written as:

$$\mathbf{j}(\mathbf{q}) = \sum_i \mathbf{j}_i(\mathbf{q}) + \sum_{i<j}\mathbf{j}_{ij}(\mathbf{q})\;, \tag{9}$$

where $\mathbf{q}$ is the momentum associated with the external EM field. In what follows, we use the notation

$$\begin{aligned}&\mathbf{k}_i = \mathbf{p}'_i - \mathbf{p}_i\;, && \mathbf{K}_i = (\mathbf{p}'_i + \mathbf{p}_i)/2\;,\\ &\mathbf{k} = (\mathbf{k}_1 - \mathbf{k}_2)/2\;, && \mathbf{K} = \mathbf{K}_1 + \mathbf{K}_2\;,\end{aligned} \tag{10}$$

where $\mathbf{p}_i$ ($\mathbf{p}'_i$) is the initial (final) momentum of nucleon i, and $\mathbf{q} = \mathbf{k}_1 + \mathbf{k}_2$ by momentum conservation.

There are two one-body operators resulting from retaining the first two terms in the $(\mathbf{p}_i/m_N)^2$ expansion of the covariant single-nucleon EM current. Of course, the leading-order term in this expansion corresponds to the non-relativistic IA operator consisting of the convection and spin-magnetization single-nucleon currents:

$$\mathbf{j}^{\rm IA} = \frac{e}{2\,m_N}\left[\,2\,e_{N,1}\,\mathbf{K}_1 + i\,\mu_{N,1}\,\boldsymbol{\sigma}_1\times\mathbf{q}\,\right]\;, \tag{11}$$

where

$$e_N = (1+\tau_z)/2\;,\;\; \kappa_N = (\kappa_S+\kappa_V\tau_z)/2\;,\;\; \mu_N = e_N+\kappa_N\;. \tag{12}$$

Here $\kappa_S = -0.12$ n.m. and $\kappa_V = 3.706$ n.m. are the isoscalar (IS) and isovector (IV) combinations of the anomalous magnetic moments of the proton and neutron, and e is the electric charge.

Two-body EM currents are constructed from a χEFT which retains as explicit degrees of freedom both pions and nucleons. The resulting operators are expressed as an expansion in nucleon and pion momenta, generically designated as Q. The leading-order (LO) contribution in Eq. (11) is of order $e\,Q^{-2}$ and contributions up to N3LO or $e\,Q^1$ are retained in the expansion. These contributions were first calculated by Park *et al.* in Ref. [18] using covariant perturbation theory. More recently, Kölling and collaborators [19], as well as some of the present authors [4–6, 20], derived them using two different implementations of time-ordered perturbation theory. In this work, we use the operators developed in Refs. [4–6, 20], where details on the derivation and a complete listing of the formal expressions may be found.

The two-body χEFT EM currents consist of long- and intermediate-range components described in terms of one-pion exchange (OPE) and two-pion exchange (TPE) contributions, respectively, as well as contact currents encoding short-range dynamics. In particular, OPE seagull and pion-in-flight currents appear at next-to-leading order (NLO) ($e\,Q^{-1}$) in the Q expansion, while TPE currents occur at N3LO. The LO and N2LO ($e\,Q^0$) contributions are given by the single-nucleon operators described above, *i.e.*, the IA operator and its relativistic correction, respectively.

At N3LO, the current operators involve a number of unknown low energy constants (LECs) which are fixed to experimental data. The LECs multiplying four-nucleon contact operators are of two kinds, namely minimal and non-minimal. The former also enter the χEFT nucleon-nucleon potential at order Q^2 and are therefore fixed by reproducing the *np* and *pp* elastic scattering data, along with the deuteron binding energy. For these, we take the values resulting from the fitting procedure implemented in Refs. [21, 22]. Non-minimal LECs (there are two of them, one multiplying an isoscalar operator and the other an isovector operator) need to be fixed to EM observables.

At N3LO, there is also an additional current of one-pion range which involves three LECs. One of these

multiplies an isoscalar structure, while the remaining two multiply isovector structures. As first observed in Ref. [18], the isovector component of this current has the same operator structure as that associated with a Δ-resonance transition current involving a one-pion exchange. In this type of two-body contribution, the external photon couples with a nucleon to excite a Δ-resonance state. The latter decays emitting a pion which is then reabsorbed by a second nucleon. Given this theoretical insight, one can impose the condition that the two isovector LECs are in fact given by the couplings of the Δ-resonance current. This mechanism is referred to as Δ-resonance saturation and has been utilized in various studies of EM observables of light nuclei (see for example [1, 6, 23–26]). Once the Δ-saturation mechanism is invoked to fix two of the unknown LECs, the resulting three LECs are fit to the deuteron and the trinucleon magnetic moments.

The values of the LECs are not unique, in that they depend on the particular momentum cutoff used to regularize the configuration-space singularities of the EM operators. In momentum space, these operators have a power law behavior for large momenta, k, which is regularized by a momentum cutoff of the form $C(k) = \exp(-k^4/\Lambda^4)$. For a list of the numerical values of the LECs for $\Lambda = 600$ MeV, which is the cutoff utilized in these calculations, we refer to Ref. [1].

The N2LO relativistic correction to the one-body IA operator involves two derivatives acting on the nucleon field. In the GFMC calculation we do not explicitly evaluate this p_i^2 term, but instead approximate it with its average value, that is $p_i^2 \sim \langle p_i^2 \rangle$, as determined from the expectation value of the kinetic energy operator in ^{8}Be, from which we obtain $\langle p_i^2 \rangle = 1.375$ fm^{-2}. This term is a small fraction of the total MEC (see, e.g., Table IV below) so the approximation has little practical effect.

To be consistent with the nomenclature utilized in Ref. [1], we denote with 'MEC' components in the EM currents beyond the IA one-body operator at LO. However, we stress that the N2LO contribution is a one-body operator, which does not involve meson-exchange mechanisms.

III. ^{8}BE ENERGY SPECTRUM

The experimental [27] and calculated GFMC energies for the ^{8}Be spectrum are presented in Table I, along with the GFMC point proton radii. The calculations were done by propagating up to some $\tau_{\rm max}$ with an evaluation of observables after every 40 propagation steps, *i.e.*, at intervals of $\tau = 0.02$ MeV^{-1}, and averaging in the interval τ=[(0.1 MeV^{-1})–$\tau_{\rm max}$]; $\tau_{\rm max}$ is typically 0.3 to 0.4 MeV^{-1}.

The calculation of the spectrum is rather involved [9], with two main challenges to face. The first originates from the resonant nature of the first two excited states (gray shaded states in Fig. 1), and the ensuing difficulty of extracting a stable resonance energy from the calculated energies which are evolving to the energy of two separated α's. This issue was addressed in Ref. [9], and more recently, however succinctly, in Ref. [10]. The last reference reported an updated measurement of the $E2$ transition between the first two excited states of ^{8}Be measured via the $\alpha + \alpha$ radiative capture with an uncertainty of $\sim 10\%$ (as opposed to the estimated $\sim 30\%$ error of previous measurements [28]). To accompany the experimental result, a GFMC calculation was performed for the $E2$ transition matrix element between the two rotational states, and between the $(2^+;0)$ state and the ground state. We reprise this calculation in more detail below.

TABLE I: GFMC ground state energy and excitations in MeV for the AV18+IL7 Hamiltonian compared to experiment [27] for the ^{8}Be spectrum. Empirical energies are obtained by unfolding the isospin-mixed experimental energies using inferred mixing coefficients (see text for explanation). Also given are the GFMC point proton (= neutron) radii in fm. Theoretical or experimental errors ≥ 1 in the last digit are shown in parentheses.

$J^\pi;T$	GFMC	Empirical	Experiment	r_p
0^+	–56.3(1)		–56.50	2.40
2^+	+ 3.2(2)		+ 3.03(1)	2.45(1)
4^+	+11.2(3)		+11.35(15)	2.48(2)
$2_2^+;0$	+16.8(2)	+16.746(3)	+16.626(3)	2.28
$2^+;1$	+16.8(2)	+16.802(3)	+16.922(3)	2.33
$1^+;1$	+17.5(2)	+17.66(1)	+17.640(1)	2.39
$1^+;0$	+18.0(2)	+18.13(1)	+18.150(4)	2.36
$3^+;1$	+19.4(2)	+19.10(3)	+19.07(3)	2.31
$3^+;0$	+19.9(2)	+19.21(2)	+19.235(10)	2.35
$0^+;2$	+27.7(2)		+27.494(2)	2.58

The second non-trivial issue is encountered when dealing with the spectrum of the isospin-mixed states at 16–19 MeV (magenta states in Fig. 1). These excited states have been extensively discussed in Ref. [11]. We compute unmixed $T = 0$ or $T = 1$ states but experimental values are of course for the mixed states. The isospin-mixing coefficients can be extracted from experimental decay widths [29]. For the 2^+ multiplet this is unambiguous, but for the 1^+ and 3^+ multiplets theoretical decay widths based on shell-model calculations have been used. This is discussed further below. In Table I we use the mixing parameters to unfold the "empirical" pure-isospin energies for comparison with our calculations, while in subsequent tables we fold the computed EM matrix elements to generate mixed matrix elements to compare to the data.

We studied the convergence of the GFMC calculations with respect to variations in the number of unconstrained steps (n_u=20 and 50) followed after the path constraint is relaxed, and found that energies, magnetic moments, and rms radii converge at $n_u = 20$, which is what is used for

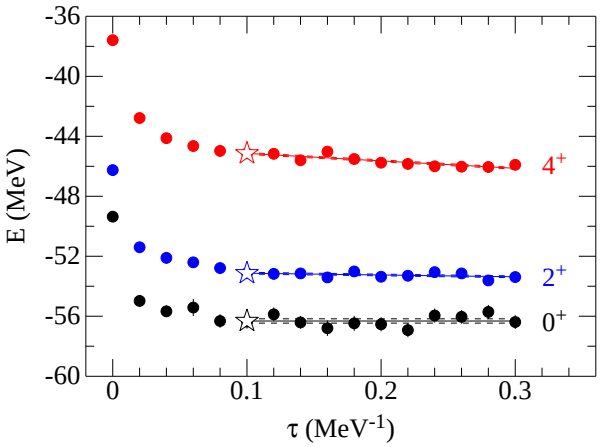

FIG. 2: (Color online) GFMC propagation in imaginary time τ of the energy expectation values of the first three states in the ^{8}Be spectrum. Black dots are GFMC propagation points for the ground state, blue dots refer to the $(2^+;0)$ rotational state at ~ 3 MeV excitation and red dots to the $(4^+;0)$ state at ~ 11 MeV excitation. Solid lines represent a linear fit to the GFMC points in the indicated time interval.

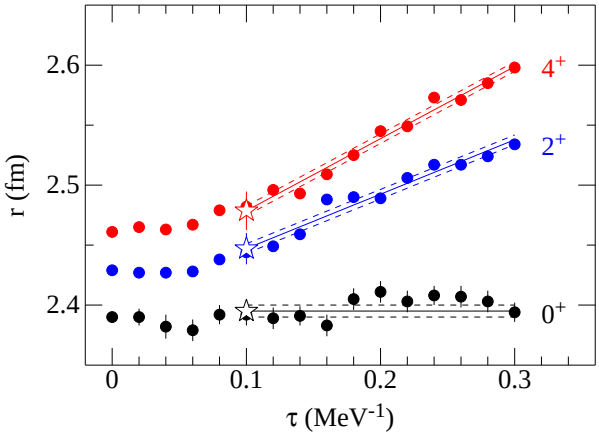

FIG. 3: (Color online) GFMC propagation in imaginary time τ of the point proton radius expectation values of the first three states in ^{8}Be spectrum; notation is the same as in Fig. 2.

the final results reported here. Most of the calculations we present are obtained by averaging two calculations, each using 50,000 walkers. For the physically narrow, nonresonant states, the energy expectation value is seen to stabilize at $\tau \sim 0.1$ MeV^{-1}.

For the physically wide, resonant states, the binding energy, magnitude of the quadrupole moment, and point proton radius all increase monotonically as τ increases. We interpret this as an indication that the system is dissolving into two separated α's. In Fig. 2, we show the GFMC propagation points for the energy expectation values of the first three states of ^{8}Be. In particular, the ground state energy is obtained with $n_u = 20$ and 20,000 walkers, while the resonant state energies are obtained using $n_u = 20$ and averaging two calculations with 50,000 walkers each. From the figure, we see that the ground state initial VMC energy expectation value at $\tau = 0$ quickly drops and reaches stability around $\tau = 0.1$ MeV^{-1} (this point is indicated in the figure with an open star). The energies of the two resonant states, instead, keep falling with time: the $(2^+;0)$ state decreases 0.25 MeV over the interval $\tau = [0.1, 0.3]$ MeV^{-1}, while the $(4^+;0)$ states falls by 1 MeV. With this declining energy there is a corresponding increase of the point proton radius expectation values, as shown in Fig. 3 and in the magnitude of the (negative) electric quadrupole moment.

Quantities associated with the resonant states have been calculated assuming that, also for these states, $\tau \sim 0.1$ MeV^{-1} is the point at which spurious contamination in the nuclear w.f.'s have been eliminated by the GFMC propagation. Thus, we make a linear fit to the GFMC values in the interval $\tau = [0.1, 0.3]$ MeV^{-1}, and extrapolate to $\tau = 0.1$ MeV^{-1} for the reported values. The choice of $\tau = 0.1$ MeV^{-1} is somewhat arbitrary. To account for this uncertainty we increase the GFMC statistical error by a systematic error that is obtained by studying the sensitivity of the results with respect to fitting procedures implemented in two different intervals, namely $\tau = [0.08, 0.3]$ MeV^{-1} and $\tau = [0.12, 0.3]$ MeV^{-1}, while keeping the same extrapolating point. The total error is represented in the figures by the dashed lines.

For the six states at 16–19 MeV excitation, the GFMC calculations are done for pure isospin states of either $T = 0$ or 1. The w.f.'s of the isospin-mixed states are written as

$$\begin{aligned} \Psi^a_J &= \alpha_J \Psi_{J,T=0} + \beta_J \Psi_{J,T=1}, \\ \Psi^b_J &= \beta_J \Psi_{J,T=0} - \alpha_J \Psi_{J,T=1}, \end{aligned} \tag{13}$$

where the mixing angles satisfy $\alpha_J^2 + \beta_J^2 = 1$. As one can see from Fig. 1 and Table I, experimentally there are two $J^\pi = 2^+$ isospin-mixed states at 16.626 and 16.922 MeV excitation energies, two $J^\pi = 1^+$ states at 17.64 and 18.15 MeV, and two $J^\pi = 3^+$ states at 19.07 and 19.235 MeV. The mixing angles are inferred from the experimental values of the decay widths. We follow the analysis carried out by Barker in Ref. [29] and update the experimental widths with more recent values to obtain the following mixing coefficients [11]:

$$\begin{aligned} &\alpha_2 = 0.7705(15), \quad \beta_2 = 0.6375(19)\,, \\ &\alpha_1 = 0.21(3), \qquad \beta_1 = 0.98(1)\,, \\ &\alpha_3 = 0.41(10), \qquad \beta_3 = 0.91(5)\,. \end{aligned} \tag{14}$$

Mixing coefficients for the 2^+ states are well known because for these states there is only one decay channel energetically open, that is the 2α emission channel, for which the experimental widths are known with $\sim 0.5\%$ accuracy. For the other isospin-mixed states, multiple decay channels are available, which makes the extraction of the mixing coefficients less direct. In addition theoretical values of $M1$ matrix elements must be used; the values above were obtained using traditional shell-model

without two-body current contributions to the matrix elements [11, 29]. Revised mixing parameters for the 1^+ pair, computed using the $M1$ matrix elements developed here, are discussed in Sec. V.

The eigenenergies of the isospin-mixed states, in Table I are given by

$$E_{a,b} = \frac{H_{00}+H_{11}}{2} \pm \sqrt{\left(\frac{H_{00}-H_{11}}{2}\right)^2 + (H_{01})^2} \quad (15)$$

where H_{00} is the diagonal energy expectation in the pure T=0 state, H_{11} is the expectation value in the T=1 state, and H_{01} is the off-diagonal isospin-mixing (IM) matrix element that connects T=0 and 1. The inferred H_{00} and H_{11} are the empirical values given in Table I.

Finally, the narrow $(0^+;2)$ state at 27 MeV excitation, which has a dominant [422] spatial symmetry, is a straightforward GFMC calculation. There could in principle be isospin-mixing with the third $(0_3^+;0)$ state in the p-shell construction of ^{8}Be, which also has [422] symmetry, via the EM and charge-dependent parts of AV18. No such state has been identified experimentally. A first VMC calculation places this state 0.7(1) MeV higher in excitation with a 125 keV IM matrix element, which predicts $\alpha_0 = 0.19(4)$ and $\beta_0 = 0.98(1)$. This small amount of mixing may still have a moderate effect on the width of the physical state, as discussed below.

The overall agreement between experiment and the calculated GFMC spectrum for AV18+IL7 shown in Table I is excellent. Only the 3^+ isospin-mixed doublet is a little too high in excitation and a little too spread out compared to the measured values.

IV. ELECTROMAGNETIC TRANSITIONS IN ^{8}BE

We present our results in terms of reduced matrix elements (using Edmonds' convention) of the $E2$ and $M1$ operators, the associated $B(E2)$ and $B(M1)$, and the resulting widths. For a transition of multipolarity λ (X designates E or M),

$$B(X\lambda) = \left\langle \Psi_{J_f} \,||X\lambda||\, \Psi_{J_i} \right\rangle^2 /(2J_i+1) \quad (16)$$

is in units of e^λ fm$^{2\lambda}$ for electric transitions and (n.m.)$^{2\lambda}$ for magnetic transitions. The widths are given by

$$\Gamma_{X\lambda} = \frac{8\pi(\lambda+1)}{\lambda[(2\lambda+1)!!]^2}\alpha\hbar c\left(\frac{\Delta E}{\hbar c}\right)^{2\lambda+1} B(X\lambda)\ , \quad (17)$$

where ΔE is the difference in MeV between the experimental initial and final state energies, E_i and E_f; α is the fine-structure constant; and $\hbar c$ is in units of MeV fm.

The calculations of electromagnetic matrix elements have been described in detail in Refs. [2, 17]. Our present results for $E2$ transitions in ^{8}Be are given in Table II where the initial and final $(J^\pi;T)$ states and the dominant associated spatial symmetries are shown in the first column and the reduced matrix elements between states of pure isospin are given in the second column. The experimental energies for the physical states are given in the third column, and the corresponding theoretical and experimental widths are shown in the fourth and fifth columns. We use the IA operator

$$E2 = e\sum_k \frac{1}{2}\left[r_k^2 Y_2(\hat{r}_k)\right](1+\tau_{kz}) \quad (18)$$

without any MEC corrections.

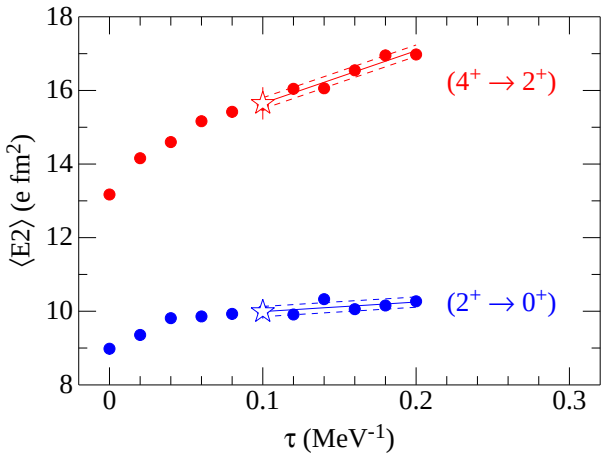

FIG. 4: (Color online) GFMC propagation in imaginary time τ of the reduced $E2$ matrix elements among the first three states in ^{8}Be spectrum; upper red dots are for the $(4^+;0) \rightarrow (2^+;0)$ transition, lower blue dots are for the $(2^+;0) \rightarrow (0^+;0)$ transition and open stars denote the extrapolated values.

In previous calculations [1, 17, 30] of nuclei in the A = 6–10 range, we have found that $E2$ matrix elements of narrow states are generally quite stable under GFMC propagation, and seldom vary much from the initial VMC estimate. However, matrix elements from wide states, e.g., for the ^{6}Li $(2^+;0) \rightarrow (0^+;0)$ decay, show a significant evolution as a function of τ. This is also true for the first two transitions in ^{8}Be from the broad rotational 2^+ and 4^+ states. The matrix element grows monotonically as the GFMC solution evolves in τ toward a separated $\alpha+\alpha$ configuration, as illustrated in Fig. 4. This growth is slow for the lower $(2^+;0) \rightarrow (0^+;0)$ transition, but much more pronounced for the upper $(4^+;0) \rightarrow (2^+;0)$ transition. Consequently, we make an extrapolation back to $\tau = 0.1 \pm 0.02$ MeV^{-1} to obtain our best estimate for the matrix element, just as we did for the energy and point proton radius discussed above in conjunction with Figs. 2 and 3. Our error estimate combines both the Monte Carlo statistical error and the uncertainty in the extrapolation point. The numerical results for these two matrix elements and corresponding decay widths Γ_{E2} are reported at the top of Table II. The transitions, which are between states of the same dominant [44] spatial symmetry, are very large and consistent with a rotor picture for ^{8}Be.

TABLE II: Calculated reduced $E2$ matrix elements and the corresponding decay widths compared to experiment [10, 27]. The various columns show 1) the initial and final $(J^\pi;T)$ states and the dominant associated spatial symmetries, 2) the GFMC matrix elements between states of pure isospin, 3) the experimental energies, and 4) the isospin-mixed theoretical and 5) experimental widths. In the width values we use the notation $[-x] = 10^{-x}$.

$(J_i^\pi;T_i) \to (J_f^\pi;T_f)$	E2[e fm^2]	E_i[MeV]$\to E_f$[MeV]	Γ_{E2}[eV]	
[s.s.]$_i$ $\to$[s.s.]$_f$			IA	Expt.
$(2^+;0) \to (0^+;0)$	10.0(2)	$3.03 \to 0.$	4.12(16)[-3]	–
$(4^+;0) \to (2^+;0)$	15.6(4)	$11.35 \to 3.03$	0.87(5)	0.67(7)
$[44] \to [44]$				
$(2_2^+;0) \to (0^+;0)$	0.55(11)	$16.626 \to 0.$	1.6(1.0)[–2]	7.0(2.5)[–2]
$(2^+;1) \to (0^+;0)$	–0.23(2)	$16.922 \to 0.$	6.2(2.0)[–2]	8.4(1.4)[–2]
$[431] \to [44]$				
$(2_2^+;0) \to (2^+;0)$	0.26(7)	$16.626 \to 3.03$	3.6(2.2)[–3]	–
$(2^+;1) \to (2^+;0)$	0.03(2)	$16.922 \to 3.03$	1.7(1.4)[–3]	–
$[431] \to [44]$				
$(1^+;1) \to (2^+;0)$	1.93(6)	$17.64 \to 3.03$	0.63(5)	0.12(5)
$(1^+;0) \to (2^+;0)$	–0.03(5)	$18.15 \to 3.03$	4.0(1.1)[–2]	–
$[431] \to [44]$				

We have also calculated an additional six $E2$ transitions from the isospin-mixed 2^+ and 1^+ doublets with dominant [431] spatial symmetry, to the $T = 0$ ground state or first 2^+ state. We denote the isospin-pure matrix elements by $E2_{T_fT_i} = \langle \Psi_{J_f,T_f} || E2 || \Psi_{J_i,T_i} \rangle$ and then use the definitions given in Eq. (13) to combine them via

$$\begin{aligned} < \Psi_{J_f,0} || E2 || \Psi^a_{J_i} > &= \alpha_{J_i} E2_{00} + \beta_{J_i} E2_{01} \ , \\ < \Psi_{J_f,0} || E2 || \Psi^b_{J_i} > &= \beta_{J_i} E2_{00} - \alpha_{J_i} E2_{01} \ , \end{aligned} \quad (19)$$

to evaluate the widths of the physical transitions for comparison to experiment. Because the $E2$ operator largely preserves spatial symmetry, these transitions are much weaker than the ones within the α-α rotational band. This makes accurate calculations of these transitions significantly more difficult.

As an example, we can compare the two $E2$ transitions from the first and second 2^+ states to the 0^+ ground state. As discussed in Refs. [31, 32], the 0^+ state has five contributing LS-coupled symmetry components: $^1S[44]$, $^3P[431]$, $^5D[422]$, $^1S[422]$, and $^3P[4211]$, with the first component having an amplitude in the present VMC starting w.f. of 0.996. The 2^+ states are linear combinations of eight components: $^1D[44]$, $^3P[431]$, $^3D[431]$, $^3F[431]$, $^5S[422]$, $^5D[422]$, $^1D[422]$, and $^3P[4211]$. The first 2^+ state also has an amplitude of 0.996 from the $^1D[44]$ component, while the second 2^+ state is dominated by the $^3P[431]$ component with an amplitude of 0.902. Consequently, 99% of the large $E2$ transition from the first excited state to the ground state is due to the matrix element between the $^1D[44]$ and $^1S[44]$ components. However, for the much smaller $E2$ transition from the second 2^+ state, this pair of components contributes 1.65 times the final result, canceled by the matrix element between the two $^3P[431]$ components, which gives -1.44 times the final result. The remaining 38 smaller terms, among which there is much additional cancellation, give 80% of the total.

Changes in these small components, which may have little effect on the energy of a given state and hence are not highly constrained by the GFMC propagation, can have a significant effect on the $E2$ matrix element. These small components may also be rather sensitive to the three-body potential in the Hamiltonian, as noted in an earlier study of $E2$ transitions in $A = 10$ nuclei [30]. This is also true for many of the $M1$ transitions discussed below, when the initial and final states have different dominant spatial symmetries.

An additional complication arises for transitions from the second 2^+ state because the GFMC propagation is not guaranteed to preserve the orthogonality of the w.f. relative to the first 2^+ state. In practice, GFMC propagation starting from orthogonal VMC w.f.'s preserves the orthogonality to a high degree [31]; in this case the amplitude $\langle \Psi^{2^+_2}(\tau) | \Psi^{2+}_V \rangle$ increases from 0.0010(7) for τ=0 to 0.040(6) averaged over $0.1 \le \tau \le 0.3$. This small admixture leaves the energy and point proton radius of the second 2^+ state as stable functions of τ, as expected for a narrow state. However, for the $E2$ matrix element from the 2^+_2 state to states of dominant [44] symmetry, there are the large cancellations discussed above and a small admixture of the the 2^+ state with its large $E2$ matrix element to states of dominant [44] symmetry can substantially affect the overlap. For this reason we have applied a correction by orthogonalizing the $\Psi^{2^+_2}(\tau)$ to Ψ^{2+}_V,

$$\Psi^{2^{+\prime}_2}(\tau) = \Psi^{2^+_2}(\tau) - \langle \Psi^{2^+_2}(\tau) | \Psi^{2+}_V \rangle \Psi^{2^+}(\tau) \, . \quad (20)$$

This reduces the mixed estimates $\langle \Psi^{2^+_2}(\tau) | E2 | \Psi^{2+}_V \rangle$ by 50% and $\langle \Psi^{2^+_2}(\tau) | E2 | \Psi^{0+}_V \rangle$ by 20%. This correction is

TABLE III: Calculated reduced $M1$ matrix elements and corresponding decay widths compared to experiment [27]. The various columns show 1) the initial and final $(J^\pi;T)$ states and the dominant associated spatial symmetries, 2) the GFMC matrix elements between states of pure isospin in IA and, 3) in total after adding MEC, 4) the % z of the total given by the MEC, 5) the experimental energies, 6) the isospin-mixed theoretical decay widths in IA and, 7) in total, and 8) experimental values. In the width values we use the notation $[-x] = 10^{-x}$. The results marked with a * or † are extra VMC calculations discussed in the text.

$(J_i;T_i) \to (J_f;T_f)$	M1[n.m.]			E_i[MeV]$\to E_f$[MeV]	Γ_{M1}[eV]		
[s.s.]$_i \to$[s.s.]$_f$	IA	Total	z		IA	Total	Expt.
$(2_2^+;0) \to (2^+;0)$	0.014(6)	0.013(6)		16.626 $\to$ 3.03	0.23(3)	0.51(6)	
$(2^+;1) \to (2^+;0)$	0.297(12)	0.447(18)	33%	16.922 $\to$ 3.03	0.30(4)	0.70(7)	
[431] $\to$ [44]				16.626 + 16.922 $\to$ 3.03	0.53(5)	1.21(9)	2.80(18)
$(1^+;1) \to (0^+;0)$	0.551(7)	0.767(9)	28%	17.64 $\to$ 0.00	6.2(2)	12.0(3)	15.0(1.8)
$(1^+;1) \to (2^+;0)$	0.398(6)	0.567(11)	30%	17.64 $\to$ 3.03	1.9(1)	3.8(2)	6.7(1.3)
$(1^+;0) \to (0^+;0)$	0.012(1)	0.014(1)		18.15 $\to$ 0.00	0.25(1)	0.50(2)	1.9(0.4)
$(1^+;0) \to (2^+;0)$	0.018(3)	0.021(3)		18.15 $\to$ 3.03	0.06(1)	0.13(2)	4.3(1.2)
[431] $\to$ [44]							
$(1^+;1) \to (2_2^+;0)$	2.287(10)	2.910(13)	21%	17.64 $\to$ 16.626	1.92(2)[–2]	2.97(3)[–2]	3.2(3)[–2]
$(1^+;1) \to (2^+;1)$	0.139(2)	0.176(3)	21%	17.64 $\to$ 16.922	1.22(3)[–3]	2.20(5)[–3]	1.3(3)[–3]
$(1^+;0) \to (2_2^+;0)$	0.167(3)	0.189(3)	12%	18.15 $\to$ 16.626	2.52(3)[–2]	2.87(3)[–2]	7.7(1.9)[–2]
$(1^+;0) \to (2^+;1)$	2.596(11)	2.887(13)	10%	18.15 $\to$ 16.922	3.26(3)[–2]	4.18(3)[–2]	6.2(7)[–2]
[431] $\to$ [431]							
$(3^+;1) \to (2^+;0)$	0.386(13)	0.622(22)	38%	19.070 $\to$ 3.03	0.87(6)	2.3(2)	10.5
$(3^+;0) \to (2^+;0)$	0.015(1)*	0.030(1)*		19.235 $\to$ 3.03	0.15(2)	0.37(4)	–
[431] $\to$ [44]							
$(0^+;2) \to (1^+;1)$	0.793(7)	1.095(8)	28%	27.49 $\to$ 17.64	6.7(1)	12.7(2)	21.9(3.9)
$(0_3^+;0) \to (1^+;1)$	0.553(3)†	0.689(3)†	21%		8.3(3)†	15.5(5)†	
$(0_3^+;0) \to (1^+;0)$	0.073(1)†	0.082(1)†	11%	27.49 $\to$ 18.15	0.28(1)†	0.54(1)†	–
[422] $\to$ [431]							

also made for corresponding $M1$ transitions discussed below, but is relatively much less important.

For the $M1$ transitions the IA matrix element is evaluated using the $M1$ operator induced by the one-body current given in Eq. (11), namely

$$\boldsymbol{\mu}^{\rm IA} = \sum_{i=1}^{A} \left(e_{N,i}\, \mathbf{L}_i + \mu_{N,i}\, \boldsymbol{\sigma}_i \right) \ , \tag{21}$$

while the one-body current at N2LO generates the following additional M1 operator terms [4]

$$\boldsymbol{\mu}^{\rm N2LO} = \ -\frac{e}{8\, m_N^3} \sum_{i=1}^{A} \Bigg[\left\{ p_i^2 \, , \, e_{N,i}\, \mathbf{L}_i + \mu_{N,i}\, \boldsymbol{\sigma}_i \right\} + e_{N,i}\, \mathbf{p}_i \times (\boldsymbol{\sigma}_i \times \mathbf{p}_i) \Bigg] \ , \tag{22}$$

where $\mathbf{p}_i = -i\nabla_i$ and $\mathbf{L}_i$ are the linear momentum and angular momentum operators of particle i, and $\{\dots\,,\dots\}$ denotes the anticommutator.

The matrix element associated with the contribution of two-body currents is

$$\langle J_f^\pi, M_f \,|\mu_z^{\rm MEC}|\, J_i^\pi, M_i\rangle = -i \lim_{q\to 0} \frac{2\, m_N}{q} \langle J_f^\pi, M_f \,|\, j_y^{\rm MEC}(q\,\hat{\mathbf{x}})|\, J_i^\pi, M_i\rangle \ , \tag{23}$$

where the spin-quantization axis and momentum transfer $\mathbf{q}$ are, respectively, along the $\hat{\mathbf{z}}$ and $\hat{\mathbf{x}}$ axes, and $M_f = M_i$. The various contributions are evaluated for two small values of $q < 0.02$ fm^{-1} and then extrapolated linearly to the limit q=0. The error due to extrapolation is much smaller than the statistical error in the Monte Carlo sampling.

In Table III, we report the results for the $M1$ transition matrix elements as well as the decay widths Γ_{M1} between the low-lying excited states. The first column specifies the initial and final states of pure isospin. The second column, labeled 'IA', shows the IA results obtained with the transition operator of Eq. (21), while the third column labeled with 'Total' shows results obtained with the complete EM current operator, Eqs. (21–23). The percentage of the total matrix element given by the MEC contributions is shown in the fourth column. The fifth column shows the energies of the physical states, while the last three columns compare the corresponding widths with the experimental data from Ref. [27].

As observed in Ref. [1], IA matrix elements are found to have larger statistical fluctuations than the MEC matrix

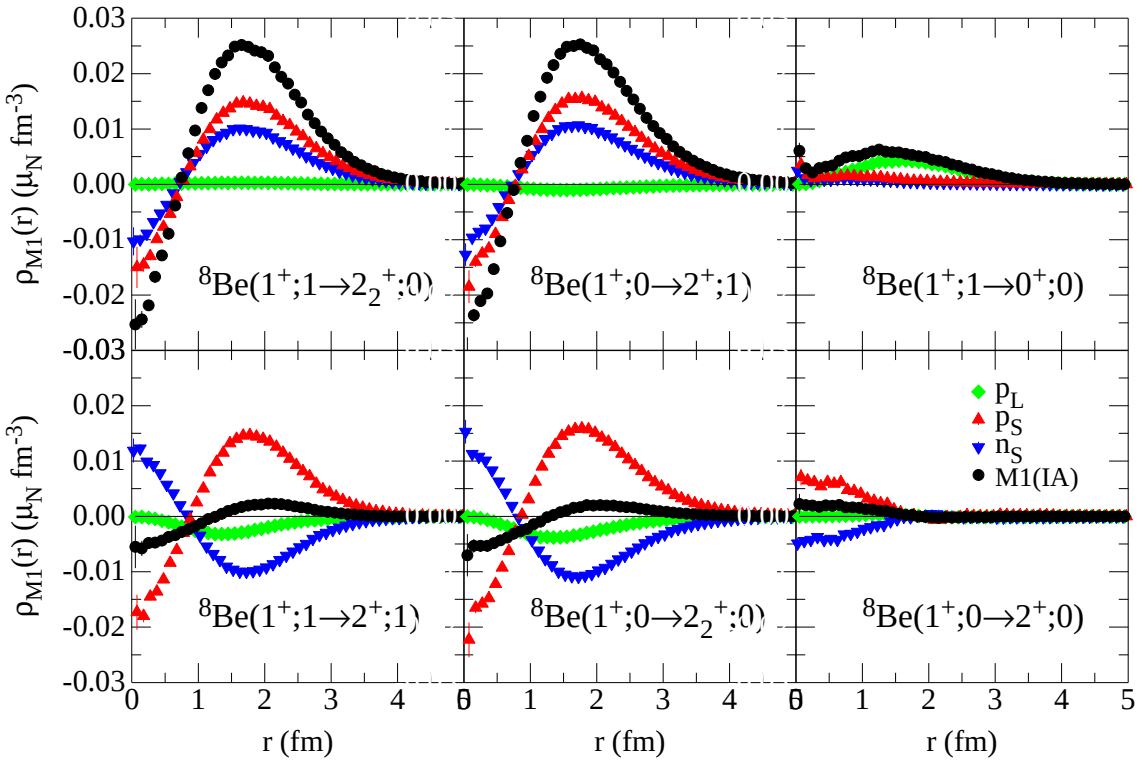

FIG. 5: (Color online) One-body (IA) $M1$ transition density in nuclear magnetons per fm^3 for selected M1 transitions (see text for explanation).

elements. We separately compute IA and MEC matrix elements, and then sum the resulting values to obtain the total numbers.

It is worthwhile noting that M1 transitions involving the resonant states do not monotonically change as τ increases, a behavior unlike the quadrupole moments, point proton radii, and energies of these states. This stability is understood by observing that the $(2^+;0)$ and $(4^+;0)$ rotational states in ^{8}Be are ∼99% pure ^{1}D$_2$[44] and ^{1}G$_4$[44] states, so they are quantized with L=2 and L=4, respectively. The orbital contribution to the magnetic moment is just L/2 nuclear magnetons because only protons contribute, *i.e.*, it is equal to 1.00 n.m. in the $(2^+;0)$ state and 2.00 n.m. in the $(4^+;0)$ state. Because it is quantized, the magnetic moment should not vary as the nucleus starts to break up in the GFMC propagation, unlike the point proton radius where r is growing as τ increases. Due to this stability, we can safely propagate M1 matrix elements involving resonant states to larger values of τ and average the GFMC result in larger τ intervals.

As for the $E2$ transitions above, the $M1$ matrix elements are evaluated between states with well defined isospin, $T = 0$ or 1. We denote these matrix elements as $M1_{T_f T_i} = \langle \Psi_{J_f,T_f} || \mu || \Psi_{J_i,T_i} \rangle$, with T_f and T_i equal to 0 or 1. For transitions involving isospin-mixing in the initial or final state, we use expressions similar to Eq.(19) to generate the physical transition rates. For transitions in which both the initial and final states are isospin-mixed, using the definitions given in Eq. (13), we obtain the following expressions for the isospin-mixed M1 transition matrix elements:

$$\begin{aligned}
< \Psi^a_{J_f} || M1 || \Psi^a_{J_i} > &= \alpha_{J_f}\alpha_{J_i} M1_{00} + \alpha_{J_f}\beta_{J_i} M1_{01} \\
&+ \beta_{J_f}\alpha_{J_i} M1_{10} + \beta_{J_f}\beta_{J_i} M1_{11} \ , \\
< \Psi^b_{J_f} || M1 || \Psi^a_{J_i} > &= \beta_{J_f}\alpha_{J_i} M1_{00} + \beta_{J_f}\beta_{J_i} M1_{01} \\
&- \alpha_{J_f}\alpha_{J_i} M1_{10} - \alpha_{J_f}\beta_{J_i} M1_{11} \ , \\
< \Psi^a_{J_f} || M1 || \Psi^b_{J_i} > &= \alpha_{J_f}\beta_{J_i} M1_{00} - \alpha_{J_f}\alpha_{J_i} M1_{01} \\
&+ \beta_{J_f}\beta_{J_i} M1_{10} - \beta_{J_f}\alpha_{J_i} M1_{11} \ , \\
< \Psi^b_{J_f} || M1 || \Psi^b_{J_i} > &= \beta_{J_f}\beta_{J_i} M1_{00} - \beta_{J_f}\alpha_{J_i} M1_{01} \\
&- \alpha_{J_f}\beta_{J_i} M1_{10} + \alpha_{J_f}\alpha_{J_i} M1_{11} \ .
\end{aligned} \tag{24}$$

The isospin-mixed M1 matrix elements are used to evaluate the widths as given in Eq. (17) for comparison to experiment. The IA and total values are reported in the sixth and seventh columns of Table III, and the experimental widths (where available) are given in the last column of the table.

Three extra transitions that were calculated only in VMC are marked by a * or † in Table III; they may affect the physical decay widths through isospin mixing. The $(3^+;0) \rightarrow (2^+;0)$ transition marked by a * is tiny and its isospin mixing has little effect on the transition from the physical 19.07 MeV state. The corresponding transition from the 19.235 MeV state is predicted to be much smaller and has not been reported experimentally.

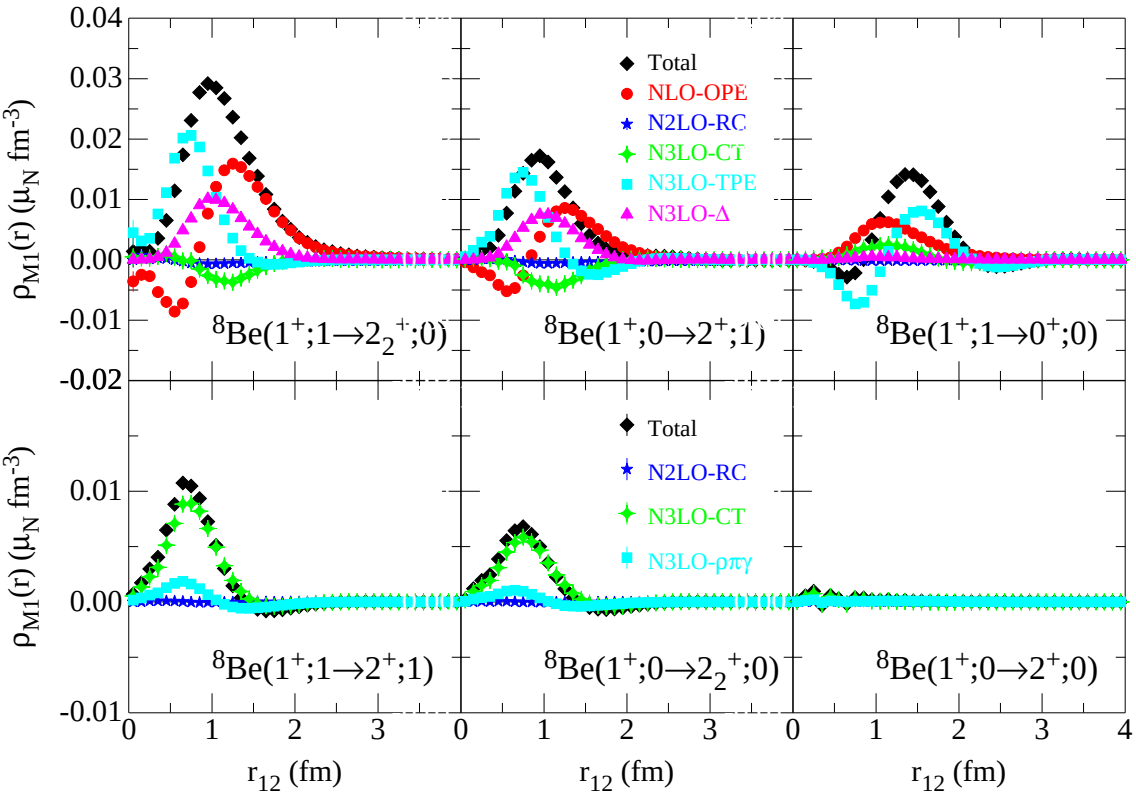

FIG. 6: (Color online) Two-body (IA) $M1$ transition density in nuclear magnetons per fm^3 for selected M1 transitions (see text for explanation).

Perhaps more interesting and important, although speculative, is the isospin mixing of the proposed $(0_3^+;0)$ state, discussed at the end of Sec. III, into the physical 27.49 MeV state, as shown in the last two lines in Table III marked by a †. The line above these gives the result assuming the physical state is pure $T = 2$, and even with MEC contributions, the theoretical width is noticeably underpredicted. The first line marked with a † shows that mixing in the $(0_3^+;0)$ state, using $\alpha_0 = 0.19(4)$, increases the decay width 20%, bringing it closer to experiment. The final line shows the corresponding decay to the 18.15 MeV state as much smaller and thus unlikely to be observed. A fourth possible transition in this group, $(0^+;2) \rightarrow (1^+;0)$, has $\Delta T = 2$ and vanishes in IA and also for the MEC considered in this paper.

The $M1$ transitions shown in Table III can be sorted into four categories, characterized by having large, medium, small, and tiny matrix elements. The two largest matrix elements are between states of the same spatial symmetry that change isospin: $(1^+;1) \rightarrow (2_2^+;0)$ and $(1^+;0) \rightarrow (2^+;1)$. All four states involved have predominant [431] spatial symmetry, so there is maximum overlap between the w.f.'s. Further, because $\Delta T = 1$, the spin-magnetization terms of the protons and neutrons add constructively. This feature is illustrated in the top left and center panels of Fig. 5, where we plot the IA contributions to the magnetic transition density from Eq.(21), evaluated with the starting VMC w.f.'s. In the figure, the red upward-pointing triangles show the proton spin contribution, the blue downward-pointing triangles show the neutron spin contribution, the green diamonds are the proton orbital term, and the black circles give the total transition density. In both these transitions, the spin contributions are large and the proton orbital piece is very small, resulting in a total matrix element of ~ 3.0 n.m.

There are also two transitions between states of the same spatial symmetry where isospin is conserved, *i.e.*, $\Delta T = 0$, which results in small matrix elements: $(1^+;1) \rightarrow (2^+;1)$ and $(1^+;0) \rightarrow (2_2^+;0)$. These are illustrated in the bottom left and center panels of Fig. 5. The magnitudes of the proton spin and neutron spin contributions are very similar to the $\Delta T = 1$ case, but they have opposite signs and cancel against each other, and there is a more substantial proton orbital term which further reduces the total, leading to matrix elements of ~ 0.2 n.m. The values of the VMC densities integrated over d^3r are given in Table IV for the transitions shown in the upper and lower left panels of Fig.5.

Next, there are five matrix elements which are between states of different spatial symmetry, and are $\Delta T = 1$ transitions, such as the $(1^+;1) \rightarrow (0^+;0)$ transition illustrated in the top right panel of Fig. 5. These transitions have proton and neutron spin contributions that add co-

TABLE IV: Individual IA and MEC contributions to one isovector and one isoscalar M1 transition matrix elements in units of n.m. calculated in VMC, corresponding to the two left-hand panels of Figs. 5 and 6.

$(J_i,T_i)\to(J_f,T_f)$	$(1^+;1)\to(2_2^+;0)$	$(1^+;1)\to(2^+;1)$
IA-p_L	0.031(1)	−0.224(1)
IA-p_S	1.442(7)	1.267(7)
IA-n_S	0.988(5)	−0.867(5)
IA Total	2.461(13)	0.176(3)
NLO-OPE	0.457(1)	
N2LO-RC	−0.059(1)	−0.001
N3LO-TPE	0.090(1)	
N3LO-CT	−0.038(1)	0.040(1)
N3LO-Δ	0.160(1)	
N3LO-$\rho\pi\gamma$		−0.008
MEC Total	0.610(2)	0.031(1)

herently, but are small because of the small overlap of the initial and final w.f.'s. However, they have larger proton orbital pieces, which also add coherently and dominate the total, leading to medium-size matrix elements in the range 0.5–1.0 n.m.

Finally, there are three matrix elements between states of different spatial symmetry that have $\Delta T = 0$, and these are tiny. An example is the $(1^+;0)\to(2^+;0)$ transition in the lower right panel of Fig. 5. In these cases the proton and neutron spin terms are small in magnitude and of opposite sign, and the proton orbital piece is also very small, resulting in matrix elements < 0.03 n.m.

The net contribution of MEC EM currents (where MEC = Total - IA) is best appreciated by looking at matrix elements between states with well-defined isospin, as given in the second to fourth columns of Table III. The quantity z in the fourth column is the percentage contribution of the MEC to the total; it is not given, if the MEC is less than the statistical error of the total. MEC contributions to $\Delta T = 0$ transitions are generally smaller than $\Delta T = 1$ transitions. This is due to the fact that the major MEC correction, given by the OPE seagull and pion-in-flight terms at NLO, is purely isovector, and cannot contribute to $\Delta T = 0$ transitions. Therefore, only higher order terms, *i.e.*, terms at N2LO and N3LO, contribute to these matrix elements, for which we find $z \sim 10\%$. Transitions induced by the isovector component of the M1 operator, that is transitions in which $T_i \neq T_f$, are instead characterized by a z factor spanning the interval $\sim 20-40\%$. In general, the NLO currents of one-pion range provide $\sim 60-70\%$ of the total MEC correction. From Table III, we see that the contribution given by the MEC currents (with only one exception) improves the IA values, bringing the theory into better agreement with the experimental data.

It is also interesting to examine the transition magnetic densities due to MEC. As examples, we discuss the same six transitions whose IA densities are given in

TABLE V: Effect of alternate isospin mixing coefficient α_1 on Γ_{M1}; the notation $[-x] = 10^{-x}$.

$E_i\to E_f$[MeV]	Γ_{M1}[eV]		
	$\alpha_1 = 0.21$	$\alpha_1 = 0.31$	Expt.
17.64 → 0.00	12.0(3)	11.4(3)	15.0(1.8)
17.64 → 3.03	3.8(2)	3.6(2)	6.7(1.3)
18.15 → 0.00	0.50(2)	1.16(4)	1.9(0.4)
18.15 → 3.03	0.13(2)	0.32(3)	4.3(1.2)
[431] → [44]			
17.64 → 16.626	2.97(3)[–2]	3.28(3)[–2]	3.2(3)[–2]
17.64 → 16.922	2.20(5)[–3]	1.39(4)[–2]	1.3(3)[–3]
18.15 → 16.626	2.87(3)[–2]	1.84(2)[–2]	7.7(1.9)[–2]
18.15 → 16.922	4.18(3)[–2]	4.59(3)[–2]	6.2(7)[–2]
[431] → [431]			

Fig. 5. The associated two-body magnetic densities obtained from MEC terms are shown in Fig. 6, again as calculated with the starting VMC w.f.'s. For the upper panels, which are isovector transitions, the red circles labeled 'NLO-OPE' show the density due to the long-ranged OPE currents, while corrections associated with TPE currents at N3LO are given by the cyan squares labeled 'N3LO-TPE'. Contact current contributions, of both minimal and non-minimal nature, are represented by the green fort symbols labeled 'N3LO-CT', while the contribution due to the current of one-pion-range, which is been saturated by the Δ-resonance, is represented by the magenta triangles labeled 'N3LO-Δ'. In the figure, we also show with blue stars labeled 'N2LO-RC' the one-body relativistic correction given in Eq. (22). The black diamonds give the sum of the various contributions. The tail of the magnetic distribution is dominated by the long-range OPE contribution, followed by the N3LO-Δ one; at intermediate- to short-range TPE contributions become important. The integrated values of the individual MEC contributions to the $(1^+;1)\to(2_2^+;0)$ isovector transition (upper left panel of Fig. 6) are listed in Table IV.

Two-body magnetic densities for the isoscalar transitions are shown in the lower panels of Fig. 6. The isoscalar component of the M1 operator has a rather different structure in comparison with that of its isovector component; it has no contributions at NLO, therefore isoscalar transitions are suppressed with respect to the isovector ones. The first correction beyond the IA picture enters at N2LO and is given by the one-body relativistic correction of Eq. (22), shown by the blue stars labeled with 'N2LO-RC'. There are two isoscalar contributions at N3LO. The first is associated with the tree-level current of one-pion range represented by the cyan squares labeled 'N3LO-$\rho\pi\gamma$'. This isoscalar tree-level current can, in principle, be saturated by the $\rho\pi\gamma$ transition current [20], however, we fix its associated LEC so as to reproduce the magnetic moments of the deuteron and the isoscalar

combination of the trinucleon magnetic moments, as explained in Sec. II. The second is the contact current at N3LO, shown by the green fort symbols labeled 'N3LO-CT', and these, in fact, dominate the total isoscalar two-body MEC contribution shown by the black diamonds. The integrated values for the $(1^+;1) \to (2^+;1)$ transition (lower left panel of Fig. 6) are also given in Table IV.

V. DISCUSSION

The spatial symmetry-conserving $M1$ transitions are between the isospin-mixed 2^+ and 1^+ doublets, so the comparison with experimental widths requires both the matrix elements between isospin-pure states and the α_J and β_J parameters of Eqs. (13,14) as input. We consider the α_2 and β_2 to be well-determined by the Γ_α measurements for the 2^+ doublet. However, the α_1 and β_1 were first estimated by Barker [29] by looking at the ratio of the Γ_{M1}'s for the 1^+ doublet and comparing to shell-model calculations. Instead, we could use our more sophisticated calculations to determine the best isospin-mixing parameters.

If we minimize the χ^2 with respect to experiment for the four spatial symmetry-conserving transitions, i.e., those given in the third block of Table III, we find $\alpha_1 = 0.31(4)$, compared to the "experimental" value of 0.21(3) used above in Table III and discussed in Ref. [11]. The predicted widths for these two isospin-mixing parameters are compared in Table V, along with the four other symmetry-changing transitions from the 1^+ doublet to the ground or first excited state; the χ^2 comparison with experiment for these cases is also improved. However, this alternate value for α_1 implies a significantly larger IM matrix element $H_{01} = -150(18)$ keV, compared to the theoretical value for this Hamiltonian of $-94(1)$ keV calculated in Ref. [11], which was in good agreement with the earlier empirical value of $-103(14)$ keV.

The results of our QMC calculations are in fair agreement with experiment when the transitions are between states of the same spatial symmetry. However, when the spatial symmetry of the initial and final states is different, we generally underpredict the reported experimental widths. The $E2$ calculations of Table II give large matrix elements for the $[44] \to [44]$ transitions and show reasonable agreement with the recently remeasured $(4^+;0) \to (2^+;0)$ width. The calculations underpredict the $[44] \to [431]$ transitions from the isospin-mixed 2^+ doublet to the ground state, although here both theory and experiment have large error bars. The predicted transitions to the first 2^+ are smaller, and perhaps not surprisingly unobserved to date. For the $E2$ transition from the first 1^+ at 17.64 MeV, we significantly overpredict the width, due to a surprisingly large $\Delta T = 1$ matrix element between $^1D[44]$ and $^1P[431]$ symmetry components. The unobserved transition from the 1^+ state at 18.15 MeV is tiny, due to a vanishing $\Delta T = 0$ matrix element. The larger value of α_1 discussed above would reduce the discrepancy with experiment slightly.

The QMC results for $M1$ matrix elements are similar, in that the four symmetry-conserving $[431] \to [431]$ transitions are in fair agreement with experiment, once MEC contributions are included. The agreement can be improved further by searching for better isospin-mixing parameters, α_J and β_J, as discussed above. Seven of the eight symmetry-changing $M1$ transitions are underpredicted by amounts ranging from only 25% to factors of 2–5. The worst matrix element is the same $(1^+;0) \to (2^+;0)$ transition that also vanishes in $E2$, leading to a decay width for the 18.15 MeV state which is 15–30 times too small.

Even though many of the experimental widths considered in this work have large errors, the serious discrepancies between some of the experimental and calculated values highlight the challenge for theory to accurately predict transition amplitudes between states with dominant admixtures of different spatial symmetry or between states consisting of linear combinations of components of different spatial symmetry and occurring with similar probabilities.

To our knowledge, Refs. [1, 2] and the present work are the only *ab initio* calculations of EM transitions in $A > 4$ nuclei that include MEC contributions. We find that the calculated $M1$ matrix elements have significant contributions, typically at the 20-30% level, from two-body EM current operators, especially from those of one-pion range. The sizable MEC corrections are found to almost always improve the IA results for $M1$ transitions. This corroborates the importance of many-body effects in nuclear systems, and indicates that an understanding of low-energy EM transitions requires contributions from MEC in combination with a complete treatment of nuclear dynamics based on Hamiltonians that include two- and three-nucleon forces.

Acknowledgments

The many-body calculations were performed on the parallel computers of the Laboratory Computing Resource Center, Argonne National Laboratory. This work is supported by the National Science Foundation, Grant No. PHY-1068305 (S.P.), and by the U.S. Department of Energy, Office of Nuclear Physics, under contracts No. DE-FG02-09ER41621 (S.P.), No. DE-AC02-06CH11357 (S.C.P. and R.B.W.) and No. DE-AC05-06OR23177 (R.S.), and under the NUCLEI SciDAC-3 grant.

[1] S. Pastore, S. C. Pieper, R. Schiavilla, and R. B. Wiringa, Phys. Rev. C **87**, 035503 (2013).

[2] L. E. Marcucci, M. Pervin, S. C. Pieper, R. Schiavilla,

and R. B. Wiringa, Phys. Rev. C **78**, 065501 (2008).
[3] L. E. Marcucci, M. Viviani, R. Schiavilla, A. Kievsky, and S. Rosati, Phys. Rev. C **72**, 014001 (2005).
[4] S. Pastore, R. Schiavilla, and J.L. Goity, Phys. Rev. C **78**, 064002 (2008).
[5] S. Pastore, L. Girlanda, R. Schiavilla, M. Viviani, and R. B. Wiringa, Phys. Rev. C **80**, 034004 (2009).
[6] M. Piarulli, L. Girlanda, L.E. Marcucci, S. Pastore, R. Schiavilla, and M. Viviani, Phys. Rev. C **87**, 014006 (2013).
[7] R. B. Wiringa, V. G. J. Stoks, and R. Schiavilla, Phys. Rev. C **51**, 38 (1995).
[8] S. C. Pieper, AIP Conf. Proc. **1011**, 143 (2008).
[9] R. B. Wiringa, S. C. Pieper, J. Carlson, and V. R. Pandharipande, Phys. Rev. C **62**, 014001 (2000).
[10] V. M. Datar *et al.*, Phys. Rev. Lett. **111**, 062502 (2013).
[11] R. B. Wiringa, S. Pastore, Steven C. Pieper, Gerald A. Miller, Phys. Rev. C **88**, 044333 (2013).
[12] R. B. Wiringa, Phys. Rev. C **43**, 1585 (1991).
[13] B. S. Pudliner, V. R. Pandharipande, J. Carlson, S. C. Pieper, and R. B. Wiringa, Phys. Rev. C **56**, 1720 (1997).
[14] N. Metropolis, A. W. Rosenbluth, M. N. Rosenbluth, A. H. Teller, and E. Teller, J. Chem. Phys. **21**, 1087 (1953).
[15] J. Carlson, Phys. Rev. C **36**, 2026 (1987); Phys. Rev. C **38**, 1879 (1988).
[16] G. P. Kamuntavičius, P. Navrátil, B. R. Barrett, G. Sapragonaite, and R. K. Kalinauskas, Phys. Rev. C **60**, 044304 (1999).
[17] M. Pervin, S. C. Pieper, and R. B. Wiringa, Phys. Rev. C **76**, 064319 (2007).
[18] T.-S. Park, D.-P. Min, and M. Rho, Nucl. Phys. **A596**, 515 (1996).
[19] S. Kölling, E. Epelbaum, H. Krebs, and U.-G. Meissner, Phys. Rev. C **80**, 045502 (2009); Phys. Rev. C **84**, 054008 (2011).
[20] S. Pastore, L. Girlanda, R. Schiavilla, and M. Viviani, Phys. Rev. C **84**, 024001 (2011).
[21] D.R. Entem and R. Machleidt, Phys. Rev. C **68**, 041001 (2003).
[22] R. Machleidt and D.R. Entem, Phys. Rep. **503**, 1 (2011).
[23] Y.-H. Song, R. Lazauskas, T.-S. Park, and D.-P. Min Phys. Lett. B 656, 174 (2007).
[24] Y.-H. Song, R. Lazauskas, and T.-S. Park, Phys. Rev. C 79, 064002 (2009).
[25] R. Lazauskas, Y.-H. Song, and T.-S. Park, Phys. Rev. C 83, 034006 (2011).
[26] L. Girlanda, A. Kievsky, L.E. Marcucci, S. Pastore, R. Schiavilla, and M. Viviani, Phys. Rev. Lett. 105, 232502 (2010).
[27] D. R. Tilley, J. H. Kelley, J. L. Godwin,D. J. Millener, J. E. Purcell, C. G. Sheu, and H. R. Weller, Nucl. Phys. A **745**, 155 (2004).
[28] V. M. Datar *et al.*, Phys. Rev. Lett. **94**, 122502 (2005).
[29] F. C. Barker, Nucl. Phys. **83**, 418 (1966).
[30] E. A. McCutchan, *et al.*, Phys. Rev. C **86**, 014312 (2012).
[31] S. C. Pieper, R. B. Wiringa, and J. Carlson, Phys. Rev. C **70**, 054325 (2004).
[32] R. B. Wiringa, Phys. Rev. C **73**, 034317 (2006).